A Low-Power Ingestible Infrared Thermal-Imaging Capsule for Functional Gastrointestinal Monitoring

Hongtao Li[1], Fengyuan Yan[1], Qi Ma[1], Chen Shen[1], Tiancheng Cao[1,2], Hen-Wei Huang[1,3]
[1]School of Electrical and Electronic Engineering, Nanyang Technological University, Singapore
[2]Department of Emergency Medicine, Brigham and Women's Hospital, Boston, USA
[3]Lee Kong Chian School of Medicine, Nanyang Technological University, Singapore
hongtao001@e.ntu.edu.sg

***Abstract*—Occult gastrointestinal (GI) lesions, including inflammation, ischemia, and early-stage neoplasia, can present as localized temperature abnormalities driven by altered perfusion and metabolism, which are not readily captured by conventional wireless capsule endoscopy (WCE). Passive thermography offers a complementary functional modality by directly measuring spatial temperature distributions within the GI tract. We present a swallowable, low-power thermal-imaging capsule integrating a long-wave infrared (LWIR) sensor array on a capsule-grade flexible printed circuit to enable spatially resolved intraluminal thermography. The system is characterized under energy-constrained operation, including the trade-off between refresh rate, thermal noise, and power consumption, and a duty-cycled acquisition strategy is adopted for long-duration monitoring. Sensor warm-up transients following re-initialization are quantified to define a stable measurement window. For operation in gastric environments, we evaluate protective LWIR windows and introduce a lightweight region-aware secondary calibration to compensate for window-induced attenuation and spatial bias. After calibration, in-field temperature residuals are constrained to within 0.1 °C. These results demonstrate the feasibility of reliable ingestible thermography under stringent power constraints and support functional monitoring of occult GI lesions.**

Keywords— wireless capsule endoscopy, ingestible thermography, passive thermal imaging, long-wave infrared (LWIR), low-power sensing, duty cycling, window calibration.

I. INTRODUCTION

Wireless capsule endoscopy (WCE), first introduced in 2001, has become a widely adopted and minimally invasive modality for small-bowel evaluation and is recommended by major clinical guidelines for conditions such as obscure gastrointestinal (GI) bleed [1–3]. Despite its clinical utility, conventional WCE remains primarily morphology-driven under white-light imaging, which can limit sensitivity when pathology manifests predominantly as functional abnormalities rather than overt mucosal defects [4]. Moreover, capsule endoscopy has recognized failure modes, including incomplete examinations and missed findings, motivating complementary ingestible sensing modalities beyond vision along [5, 6]

Tiancheng Cao is supported by the Wendy and Eric Schmidt AI in Science Postdoctoral Fellowship. This work is supported by the Nanyang Assistant Professorship and A*STAR MedTech MTC Programmatic Seed Fund (M24N9b0125) *(Hongtao Li and Fengyuan Yan contributed equally to this work.)*

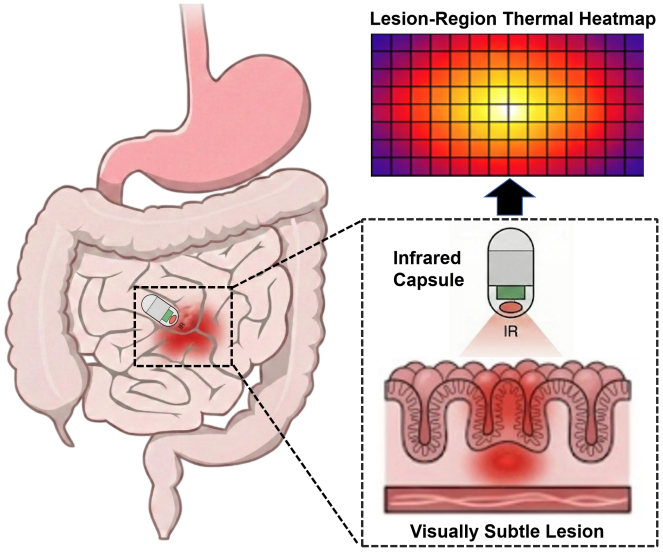

Fig. 1. Concept of ingestible thermal mapping for lesion localization.

Thermal imaging provides a functional diagnostic dimension by mapping temperature distributions governed by tissue perfusion and metabolism. In the GI tract, thermography has been investigated for lesion assessment in malignancy, inflammation, and ischemia, where degree-scale temperature differences have been reported between normal and pathological tissue [7–9]. Infrared-based approaches have also demonstrated label-free discrimination of tumor tissue when visual cues are subtle [10] These findings motivated spatially resolved thermography as a complementary capable of revealing physiologically meaningful contrast that may be absent n conventional white-light capsule imaging.

Building on this motivation, present an ingestible infrared thermal-imaging capsule that augments conventional WCE by capturing spatially resolved intraluminal temperature patterns associated with perfusion and metabolic anomalies. As illustrated in Fig. 1, the capsule traverses the GI tract and acquires local thermograms that provide quantitative functional contrast for lesion localization beyond purely morphological inspection.

Translating thermography into a swallowable capsule, however, poses significant engineering challenges. Ingestible devices must operate under stringent constraints on size, power, safety, and deployability [6, 11]. While existing ingestible

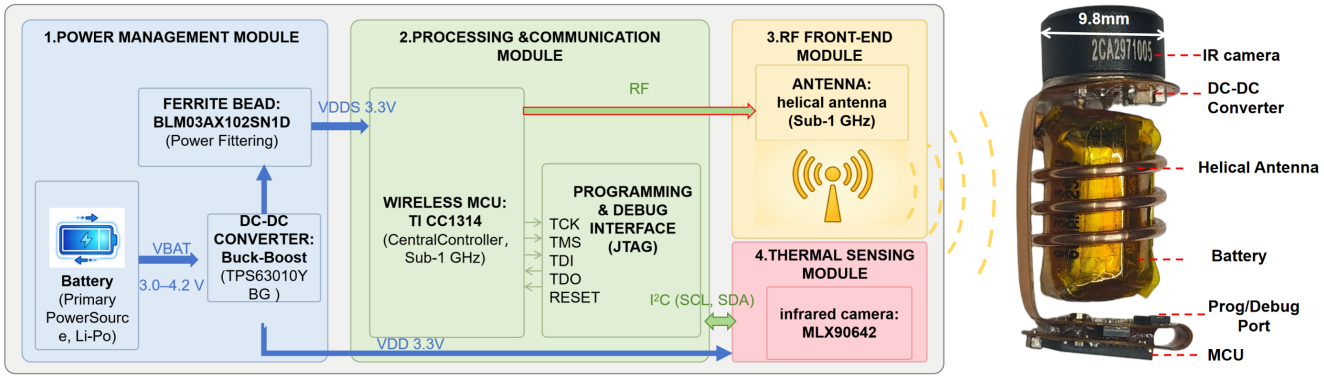

Fig. 2. System overview of the ingestible LWIR capsule platform.

temperature sensors provide reliable scalar thermometry [12], they do not capture spatial thermal information. Furthermore, uncooled long-wave infrared (LWIR) sensors exhibit finite thermal time constants, warm-up transients, and sensitivity to packaging-induced radiometric distortion, all of which can compromise quantitative accuracy and spatial consistency if not carefully managed [13–16].

To address these challenges, this work makes three contributions: (i) we develop a capsule-grade LWIR theraml-imaging platform and a benchtop characterization framework to quantify the refresh-rate-dependent trade-off between noise and power consumption; (ii) we characterize repeatable warm-up transients under duty-cycled operation and define a stable acquisition window for reliable measurement; and (iii) we introduce a lightweight, region-aware secondary calibration method to compensate for window-induced attenuation and field-dependent bias, improving quantitative accuracy and spatial consistency of ingestible thermograms.

II. METHODOLOGY

A. Experimental Setup and Data Acquisition

A capsule-grade LWIR thermal-imaging platform was developed for ingestible sensing, as summarized in Fig. 2. The system integrates four functional modules: power management for regulated 3.3 V operation from a Li-ion source, a low-power SoC (TI CC1314) composed of an MCU and a sub-1 GHz RF front-end, a helical antenna for telemetry, and an LWIR thermal-sensing module based on the MLX90642 array with a resolution of 32 x 24 pixels. A benchtop measurement setup was built to evaluate noise, power, warm-up dynamics during mode entry, and window-induced bias. The sensorized capsule-grade FPC faces a temperature-controlled infrared calibration furnace (static target) at a fixed standoff distance of 9 mm, and thermal frames are streamed to a PC via XDS110 UART. System power is supplied and logged using a Nordic PPK2 configured at 3.7 V to emulate a Li-ion battery. An on-board DC–DC converts the battery input to 3.3 V for the MCU and the MLX90642 array. Unless otherwise stated, each operating condition is recorded for 10 minutes; for quantitative analysis, we use the last 400 stable frames.

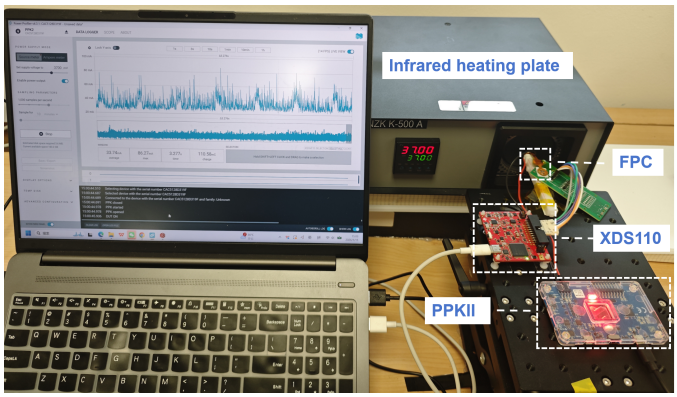

Fig. 3. Benchtop setup for thermal and power logging.

B. Noise and Power Versus Refresh Rate

To quantify the static noise–power trade-off, we sweep the MLX90642 refresh rate from 2 to 16 Hz. For each refresh-rate setting, the MCU is reconfigured accordingly, and a separate 10-minute run is recorded. During each run, thermal frames are streamed to a PC via UART while the total system input power is simultaneously logged by the PPK2 (Fig. 3).

All measurements are conducted under a static scene: the sensorized capsule-grade FPC is held at a fixed standoff distance of 9 mm from the infrared calibration furnace, and the furnace setpoint is kept constant across all runs. To ensure fair comparison across refresh rates, we discard the initial post-startup transient and compute all quantitative metrics using the last $N = 400$ frames of each 10-minute log, corresponding to the steady-state segment.

Let $T_p(k)$ denote the reported temperature of pixel p at frame index k within the stable segment. For each pixel, the temporal mean and RMS noise are

$$\bar{T}_p = \frac{1}{N}\sum_{k=1}^{N} T_p(k),$$
$$\mathrm{RMS}_p = \sqrt{\frac{1}{N}\sum_{k=1}^{N}\left(T_p(k) - \bar{T}_p\right)^2}, \tag{1}$$

where N is the number of frames used in the stable segment (in this study, $N = 400$). We further report the average noise across all 768 pixels:

$$\mathrm{RMS}_{\mathrm{avg}} = \frac{1}{768} \sum_{p=1}^{768} \mathrm{RMS}_p. \tag{2}$$

This definition isolates per-pixel temporal noise under a static scene by subtracting each pixel's mean $\bar{T}_p$ to remove fixed offsets, and characterizing the residual fluctuations via their RMS. We then compare system power and $\mathrm{RMS}_{\mathrm{avg}}$ across refresh rates as the primary evaluation metrics.

C. Duty-Cycling for Low-Power Operation and Warm-Up Stability

To support long-duration operation under a constrained battery budget, duty-cycling is adopted as the primary low-power operating mode. We evaluate the resulting average power consumption and achievable battery lifetime under representative duty-cycling schedules. However, repeated transitions between sleep and active states require re-enabling and re-initializing the MLX90642, which introduces a repeatable warm-up transient that biases the initial frames following each wake-up.

To characterize this behavior, duty-cycled experiments are conducted at frame rates of 2 Hz and 8 Hz using a symmetric 50% on/off schedule (50 frames ON followed by 50 frames OFF). The firmware emits a UART marker at each ON/SLEEP transition, enabling precise cycle-aligned analysis. Warm-up behavior is quantified by tracking the frame-averaged temperature as a function of elapsed time (or cycle index) after each wake-up event.

Stability is defined as the point at which the measured temperature remains within $\pm 0.05\,^{\circ}\mathrm{C}$ of its steady-state value. To suppress spurious detections due to noise, this condition must be satisfied for five consecutive samples. The earliest time point meeting this criterion is designated as the onset of thermal stability, and the corresponding frame index is denoted as N_{wu}. Warm-up frames acquired prior to N_{wu} are excluded from subsequent analyses.

D. Ge/DLC Window Secondary Calibration

To enable reliable LWIR thermography in the harsh GI environment with pH ranging from 1 to 7 and 100% humidity, the capsule must be hermetically sealed with a protective infrared window. This packaging inevitably perturbs the radiometric measurement path and can introduce both attenuation and spatially varying bias across the field of view (FOV). Mechanistically, finite window transmittance attenuates the target radiance and biases temperature readings downward, whereas the window's self-emission and its surface reflection of ambient/background radiation introduce additional radiance terms that can cause systematic errors if uncorrected. In addition, Fresnel reflections at the interfaces and multiple internal reflections within the window can couple stray radiance, resulting in a spatially non-uniform bias across the FOV [17, 18].

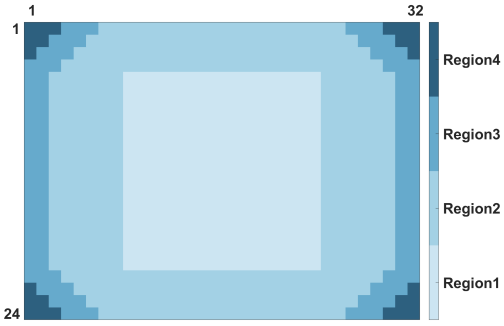

Fig. 4. Four-region mask (R1–R4) for region-aware analysis.

These window-induced errors become more pronounced as the reference temperature increases and radiance rises [18].

To compensate for these window-induced artifacts, we evaluate two infrared-window configurations for two complementary purposes. First, Ge/DLC is the intended optics for future gastric deployment, as it provides the mechanical and biochemical robustness required for in-vivo use and thus represents the practical end configuration. Second, we additionally test a ZnSe window as a material "stress test" to verify that the proposed calibration is not over-specialized to a single window material, but instead generalizes across different spectral transmission and radiometric attenuation characteristics. To ensure a fair, apples-to-apples comparison, both window conditions use the same region-aware model structure and the same hyperparameter-selection protocol; only the model coefficients are fitted independently for each window type. To compensate for these window-induced artifacts with low model complexity, we adopt a region-aware strategy: the 32×24 frame is partitioned into four regions (center, remaining area, side bands, and corner triangles; Fig. 4). For each region r, we use the region-mean raw temperature G_r and the on-chip temperature channel T_s (defined as $T_s \triangleq T_a$) to predict the calibrated temperature $\hat{T}$:

$$\begin{aligned} \hat{T} = c_0 + c_1 T_s + c_2 G_r + c_3 T_s^2 + c_4 G_r^2 \\ + k_1 \sin(\omega G_r) + k_2 \cos(\omega G_r), \end{aligned} \tag{3}$$

where $\omega = 2\pi/P$ and P is the ripple period. We observed that the residual as a function of the raw region-mean temperature exhibits a small but repeatable ripple-like pattern; to avoid introducing an overly complex model, we include a harmonic basis pair $\sin(\omega G_r)$ and $\cos(\omega G_r)$ as a lightweight correction term. Ridge regularization is applied after standardizing the features, while the intercept is left unpenalized. The ridge coefficient λ is selected per region using a train-only leave-one-temperature-out procedure. Among models whose validation RMSE is within 1% of the best, we choose the one with the smallest coefficient norm to favor stability. This region-aware secondary calibration serves as a practical correction stage after window integration, improving radiometric consistency across the FOV without resorting to per-pixel high-order models.

III. RESULTS AND DISCUSSION

A. Noise–Power Trade-off

Fig. 5 shows that increasing the refresh rate simultaneously raises power consumption and noise. The line plot indicates that the system input power increases markedly with refresh rate, from 125 mW at 2 Hz to approximately 160 mW at 16 Hz. Meanwhile, the gray box plots show that pixel-wise temporal noise increases overall with frequency: the mean noise $\mathrm{RMS}_{\mathrm{avg}}$ rises from about 0.06 °C at 2 Hz to about 0.13 °C at 16 Hz, and the dispersion widens accordingly—the interquartile range increases from roughly 0.01 °C to about 0.05 °C—indicating that higher refresh rates not only elevate the average noise level but also exacerbate pixel-to-pixel non-uniformity. The noise heatmaps further reveal pronounced spatial non-uniformity: each pixel value represents its temporal noise RMS_p computed over a stable segment of $N = 400$ frames (see Methods). Noise differs systematically across the field of view, with the center region (Region 1) exhibiting the lowest noise and the corner region (Region 4) the highest. Moreover, as the refresh rate increases, noise rises not only globally but also at different rates across regions, following a clear trend that pixels closer to the edges and corners exhibit larger increases. For example, at 2 Hz the noise levels across all four regions are lower and more uniform (typically within 0.05–0.10 °C). At 8 Hz, edge/corner noise becomes noticeably higher than the center, whereas Region 2 and Region 3 remain relatively close to Region 1 (within approximately 0.05 °C). At 16 Hz, this spatial imbalance becomes more severe: peripheral noise can approach 0.2 °C while the center remains below 0.1 °C, which can confound local temperature-contrast interpretation in thermograms and reduce the reliability of lesion-related temperature detection.

Under stringent energy constraints for continuous monitoring, operating at 2 Hz yields the lowest power consumption while maintaining the lowest noise floor, making it a suitable baseline configuration. However, the limited temporal resolution at 2 Hz reduces the ability to capture short-lived thermal dynamics and can exacerbate motion-induced variability when the capsule experiences transient changes in pose and distance. Based on the observed noise–power trade-off and spatial noise distribution, these results motivate a two-mode refresh-rate scheduling strategy for future capsule designs: operate at 2 Hz during routine scanning to reduce average power and maintain more stable, uniform thermograms, and temporarily switch to 8 Hz upon suspected thermal anomalies to capture richer temporal dynamics at a more controlled noise cost. Compared with 16 Hz, 8 Hz provides sufficient temporal bandwidth for motion-robust feature extraction and sequence-based analysis while incurring a more moderate noise increase, thereby balancing information gain and energy overhead.

In intended deployment, the capsule remains in a low-power sleep state during gastric residence and operates primarily in the small intestine. Using an 08120 Li-ion cell (60 mAh at 3.7 V; energy ≈ 0.222 Wh), with measured power $P_{2\mathrm{Hz}} = 125$ mW and $P_{8\mathrm{Hz}} = 146$ mW and an 8 Hz trigger fraction

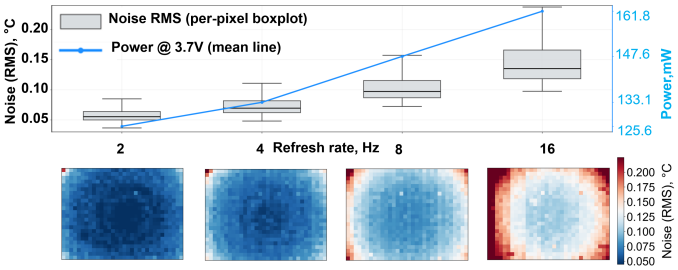

Fig. 5. Noise (per-pixel RMS) and system power versus refresh rate, with representative noise maps.

TABLE I
ESTIMATED RUNTIME VERSUS ACTIVE-DUTY FRACTION δ.

Active duty δ (%)	Estimated runtime t (h)
20	8.78
30	5.86
40	4.40
60	2.93
80	2.20
100	1.76

$\alpha = 5\%$, the average power can be expressed as $P_{\mathrm{avg}} = (1-\alpha)P_{2\mathrm{Hz}} + \alpha P_{8\mathrm{Hz}} \approx 126.05$ mW; assuming the capsule operates continuously at this average power level, the corresponding runtime is estimated as $t \approx 0.222/0.12605 \approx 1.76$ h.

B. Duty-Cycled Runtime Estimation and Warm-Up Stabilization

To cover the small-bowel transit time, its typical clinical time scale is usually on the order of approximately 3–5 h, whereas our estimated continuous active runtime is only 1.76 h, which is clearly insufficient. Therefore, we further estimate the system endurance under a duty-cycled dual-mode operating framework, where the system alternates between an active acquisition state and a low-power sleep state.

Let δ denote the active-duty fraction. The measured sleep current is $I_{\mathrm{sleep}} = 25\ \mu$A (at 3.7 V supply), corresponding to a sleep power of $P_{\mathrm{sleep}} = 0.0925$ mW. The average system power is then

$$P_{\mathrm{avg}} = \delta P_{\mathrm{active}} + (1-\delta)P_{\mathrm{sleep}}, \tag{4}$$

and the corresponding runtime can be estimated as $t \approx E/P_{\mathrm{avg}}$, where E is the available battery energy. Table I summarizes the endurance estimates under several representative duty-cycle settings. As expected, reducing δ increases endurance approximately proportionally: under continuous operation ($\delta = 100\%$), the runtime is 1.76 h, while under the same dual-mode assumption, the runtime can be extended to 5.86 h when $\delta = 30\%$.

Under duty-cycled operation, each wake-up that re-enables and re-initializes the sensor induces a repeatable warm-up transient. Fig. 6 shows the post-enable warm-up responses at 2 Hz and 8 Hz, where the horizontal axis is time converted from the frame index at the corresponding refresh rate. Following re-initialization, the frame-mean temperature rises rapidly and then converges to a stable plateau.

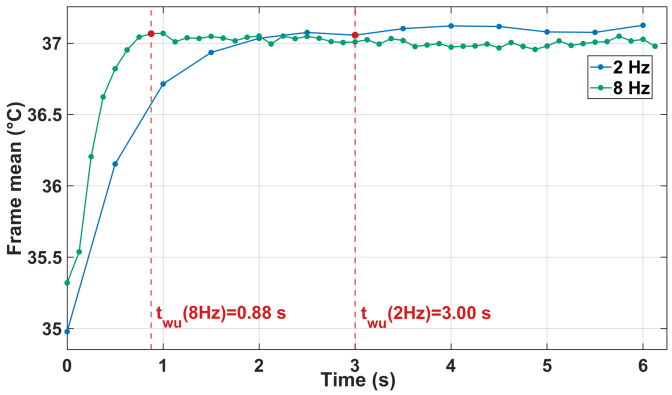

Fig. 6. Post-enable warm-up after re-initialization (2 Hz and 8 Hz).

Importantly, the transient-to-steady behavior is highly repeatable, enabling a practical and reproducible definition of the stabilization time. Based on the stability criterion, the stabilization times are $T_{\mathrm{wu}} = 0.88$ s (7 frames) at 8 Hz and $T_{\mathrm{wu}} = 3.00$ s (6 frames) at 2 Hz. Accordingly, after each wake-up, we discard the first $N_{\mathrm{wu,8Hz}}$ frames in 8 Hz mode and the first $N_{\mathrm{wu,2Hz}}$ frames in 2 Hz mode to avoid transient-induced bias, ensuring that subsequent analysis is performed within a predictable stable window. This strategy supports energy savings via duty cycling while maintaining reliable temperature readout across refresh-rate modes.

C. Window Calibration Improves Spatial Bias (Ge/DLC and ZnSe)

Ge/DLC is the intended configuration for future gastric use, while ZnSe is included as a cross-material generality check. To ensure radiometric consistency during operation. we quantify the spatial residual behavior before and after the Ge/DLC secondary calibration. Region-wise residual statistics are summarized in Fig. 7, and representative thermal maps are shown in Fig. 8.

In the raw windowed measurements, the residuals exhibit an increasingly negative bias and a larger spread at higher reference temperatures, with the effect being most pronounced in peripheral regions. For example, around physiologically relevant temperatures (approximately 37°C), the bias is approximately 0.25°C in Region 1, increases to approximately 0.4°C in Regions 2/3, and further degrades to approximately 0.6°C in Region 4. This pattern indicates spatially non-uniform attenuation and radiance coupling introduced by the windowed optical path, leading to field-of-view (FOV) dependent offsets that can degrade quantitative interpretation.

After applying the region-aware ridge + ripple compensation, the mean residuals are pulled closer to zero and the interquartile ranges contract across regions, demonstrating improved radiometric consistency and reduced spatially structured error over the FOV. This improvement is visually evident in Fig. 8 and quantitatively summarized in Table II. Specifically, at a 37.5°C blackbody reference, before calibration both Ge/DLC and ZnSe windowed measurements exhibit an overall downward shift (attributable to transmittance loss)

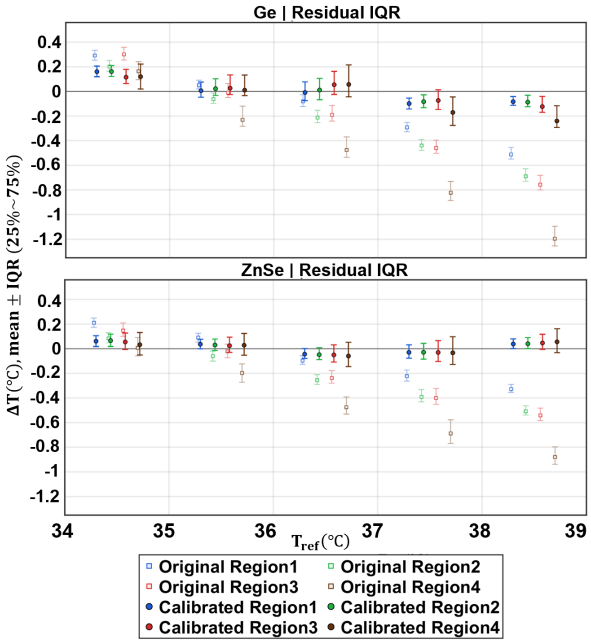

Fig. 7. Residual mean and IQR before/after calibration (Ge/DLC).

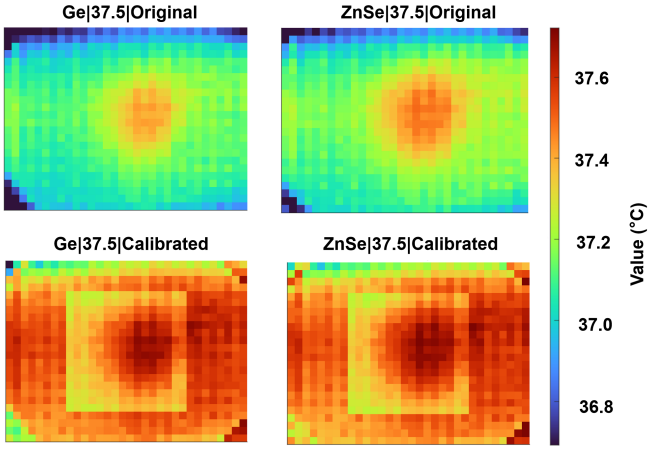

Fig. 8. Example maps before/after calibration (Ge/DLC and ZnSe).

and an increasing center-to-edge deviation, reflecting degraded spatial uniformity. Table II further shows that the raw region-wise errors are consistently negative and increase toward the periphery, with the largest error in Region 4 (Ge/DLC: -0.825°C; ZnSe: -0.690°C). After secondary calibration, the center-to-edge gradient is substantially reduced and region-wise readings move closer to the reference: for Ge/DLC, Regions 1–3 contract to within 0.05°C (from -0.049 to -0.040°C), while Region 4 remains larger at -0.145°C but still improves markedly from -0.825°C; for ZnSe, all regions tighten to within 0.035°C (from -0.031 to -0.035°C). We note that, due to the piecewise region-wise modeling, a mild discontinuity may appear at the Region 1/Region 2 boundary; however, its magnitude is typically within 0.2°C and is acceptable for our application.

TABLE II
REGION-WISE TEMPERATURE ERROR RELATIVE TO 37.5 °C.

Tref	Window	Condition	$\Delta R1$	$\Delta R2$	$\Delta R3$	$\Delta R4$
37.5°C	Ge	Original	-0.298	-0.445	-0.464	-0.825
		Calibrated	-0.049	-0.015	-0.040	-0.145
	ZnSe	Original	-0.225	-0.393	-0.402	-0.690
		Calibrated	-0.032	-0.031	-0.033	-0.035

IV. CONCLUSION

This work demonstrates a swallowable, low-power passive thermal-imaging capsule capable of spatially resolved LWIR, enabling temperature maps to serve as a functional cue for detecting and localizing occult GI abnormalities. The system integrates an MLX90642 thermal array on a capsule-grade FPC with low-power control and telemetry, supported by a benchtop characterization workflow and lightweight correction methods suitable for embedded deployment. Experimental results reveal a clear refresh-rate–dependent noise–power trade-off (125 mW at 2 Hz vs. 146 mW at 8 Hz) and spatially non-uniform temporal noise, motivating a practical two-mode operation strategy with a low-power 2 Hz baseline and event-triggered 8 Hz bursts. Under duty-cycled operation, the estimated runtime reaches 5.86 h at a 30% duty cycle, and repeatable wake-up transients stabilize within 0.88 s at 8 Hz and 3.00 s at 2 Hz, enabling a simple prefix-discard rule for reliable acquisition. For capsule-compatible LWIR packaging, a region-aware secondary calibration compensates window-induced attenuation and field-dependent bias, constraining in-FOV temperature error to approximately 0.1 °C under representative conditions. Together, these results establish the feasibility of reliable, energy-efficient ingestible thermography and provide a system foundation for functional GI monitoring beyond conventional morphology-based capsule endoscopy. Future work will focus on validation under realistic GI motion and standoff variability, on-device triggering for adaptive frame-rate switching, and further optimization of embedded buffering, compression, and telemetry to maximize thermographic information per joule.

REFERENCES

[1] G. Iddan, G. Meron, A. Glukhovsky, and P. Swain, "Wireless capsule endoscopy," *Nature*, vol. 405, no. 6785, p. 417, May 2000.

[2] M. Pennazio *et al.*, "Small-bowel capsule endoscopy and device-assisted enteroscopy for diagnosis and treatment of small-bowel disorders: European Society of Gastrointestinal Endoscopy (ESGE) clinical guideline," *Endoscopy*, vol. 47, no. 04, pp. 352–376, 2015.

[3] S. C. Zammit *et al.*, "Optimising the use of small bowel endoscopy: a practical guide," *Frontline Gastroenterology*, vol. 10, no. 2, pp. 171–176, Apr. 2019.

[4] A. Moglia *et al.*, "Capsule endoscopy: Progress update and challenges ahead," *Nature Reviews Gastroenterology & Hepatology*, vol. 6, no. 6, pp. 353–362, 2009.

[5] E. Rondonotti *et al.*, "Complications, limitations, and failures of capsule endoscopy: a review of 733 cases," *Gastrointestinal Endoscopy*, vol. 62, no. 5, pp. 712–716, Nov. 2005.

[6] P. A. Thwaites *et al.*, "Review article: Current status and future directions of ingestible electronic devices in gastroenterology," *Alimentary Pharmacology & Therapeutics*, vol. 59, no. 4, pp. 459–474, Feb. 2024.

[7] C. Stefanadis *et al.*, "Thermal heterogeneity constitutes a marker for the detection of malignant gastric lesions in vivo," *Journal of Clinical Gastroenterology*, vol. 36, no. 3, pp. 215–218, 2003.

[8] M. Banić *et al.*, "Thermography in patients with inflammatory bowel disease and colorectal cancer: evidence and review of the method," *Periodicum Biologorum*, vol. 113, no. 4, pp. 439–444, 2011.

[9] O. Malafaia *et al.*, "Infrared imaging contribution for intestinal ischemia detection in wound healing," *Acta Cirúrgica Brasileira*, vol. 23, no. 6, pp. 511–519, Nov. 2008.

[10] S. Kim *et al.*, "Infrared thermal modulation endoscopy for label-free tumor detection," *Scientific Reports*, vol. 14, p. 31575, Dec. 2024.

[11] G. Pan and L. Wang, "Swallowable wireless capsule endoscopy: Progress and technical challenges," *Gastroenterology Research and Practice*, vol. 2012, p. 841691, 2012, article ID 841691.

[12] F. Huang, C. Magnin, and P. Brouqui, "Ingestible sensors correlate closely with peripheral temperature measurements in febrile patients," *Journal of Infection*, vol. 80, no. 2, pp. 161–166, Feb. 2020.

[13] H. Budzier and G. Gerlach, "The challenges of using an uncooled microbolometer array in a thermographic application," in *Proceedings of SPIE*, vol. 4710, 2002, pp. 535–544.

[14] S. Poirier, C. Alain, and P. Topart, "Measurement of thermal time constant of microbolometer arrays," *Optics Letters*, vol. 38, no. 6, pp. 992–994, 2013.

[15] R. Usamentiaga *et al.*, "Infrared thermography for temperature measurement and non-destructive testing," *Sensors*, vol. 14, no. 7, pp. 12 305–12 348, 2014.

[16] P. W. Nugent, J. A. Shaw, and N. J. Pust, "Correcting calibrated infrared sky imagery for the effect of an infrared window," *Journal of Atmospheric and Oceanic Technology*, vol. 26, pp. 2403–2410, Nov. 2009.

[17] S. Vujić *et al.*, "Optical protective window design and material selection issues in the multi-sensor electro-optical surveillance systems," *Sensors*, vol. 23, no. 5, p. 2784, 2023.

[18] H.-Y. Pan *et al.*, "Simulation of stray radiation from optical window with temperature-dependent spectral properties," *Applied Optics*, vol. 60, no. 22, pp. 6695–6705, 2021.